



**HAL**  
open science

# Stochastic Optimization of Targeted Energy Transfer with Time-Dependent Cubic Nonlinearity

Aurélie Labetoulle, Samy Missoum, Emmanuel Gourdon, Alireza Ture  
Savadkoohi

► **To cite this version:**

Aurélie Labetoulle, Samy Missoum, Emmanuel Gourdon, Alireza Ture Savadkoohi. Stochastic Optimization of Targeted Energy Transfer with Time-Dependent Cubic Nonlinearity. *Communications in Nonlinear Science and Numerical Simulation*, 2024, 139, pp.108314. 10.1016/j.cnsns.2024.108314 . hal-04681657

**HAL Id: hal-04681657**

**<https://hal.science/hal-04681657v1>**

Submitted on 29 Aug 2024

**HAL** is a multi-disciplinary open access archive for the deposit and dissemination of scientific research documents, whether they are published or not. The documents may come from teaching and research institutions in France or abroad, or from public or private research centers.

L'archive ouverte pluridisciplinaire **HAL**, est destinée au dépôt et à la diffusion de documents scientifiques de niveau recherche, publiés ou non, émanant des établissements d'enseignement et de recherche français ou étrangers, des laboratoires publics ou privés.



# Stochastic Optimization of Targeted Energy Transfer with Time-Dependent Cubic Nonlinearity

A. Labetoulle<sup>a</sup>, S. Missoum<sup>b</sup>, E. Gourdon<sup>a</sup>, A. Ture Savadkoochi<sup>a</sup>

<sup>a</sup>*ENTPE, Ecole Centrale de Lyon, CNRS, LTDS, UMR5513, Vaulx-en-Velin  
Cedex, 69518, France*

<sup>b</sup>*Aerospace and Mechanical Engineering Department. The University of  
Arizona, Tucson, Arizona, 85721, USA*

## Abstract

The stochastic optimization of a nonlinear energy sink (NES) with a time-dependent stiffness is considered. The NES is linearly coupled to a main system. The optimization aims to find the stiffness properties of the NES that minimize the expected value of the velocity of the main system while accounting for the statistical distributions of the excitation amplitude and frequency. It is shown that the system's responses are highly sensitive to uncertainty and can even exhibit a discontinuous behavior. This represents a major hurdle for the optimization, which is already hampered by the potentially large computational cost associated with the time integrations. To tackle the high-sensitivity to uncertainties and reduce the computational burden, a dedicated surrogate-based stochastic optimization algorithm is used. Specifically, the approach uses Kriging surrogates built from the unsupervised identification of clusters resulting from response discontinuities. Comparisons between efficiencies of optimal nonlinear absorbers with and without time-dependent stiffness are performed and discussed.

## 1. Introduction

The safety of mechanical and structural components and the comfort of their users require the design of appropriate noise and vibration mitigation systems [1, 2]. This can be achieved by various active to passive strategies [3, 4]. Active control [5] requires sensors, actuators, and external sources to modify the responses of the main system to applied external forces. The passive mitigation [3] of a system is achieved using one or several oscillators linearly



or nonlinearly coupled to the main system. In the domain of mechanical vibrations, the tuned mass damper [6] and its derived technologies such as the tuned liquid damper [7], are examples of passive linear approaches. In acoustics, Helmholtz resonators [8] in the linear domain [9], are another example of linear passive noise mitigation technique. Linear mitigation systems are very efficient around the tuned frequency of the main system. However, their efficiency is markedly reduced for other frequency bands. It is therefore essential to account for this limitation when the frequencies of the main system vary in time. Such variations can be due to damage accumulation or nonlinearities in the main system. Roberson [10] showed that by adding a cubic term to the restoring force of an absorber, its efficiency can be expanded to larger frequency bands than the linear absorber. To take advantages of nonlinearities, many types of nonlinear absorbers have been developed. Among them, the Nonlinear Energy Sink (NES) [11, 12] is characterized by a pure nonlinear stiffness leading to a so-called Targeted Energy Transfer (TET) [13, 14]. A TET is based on the channeling back and forth of vibratory energies between coupled oscillators with amplitude-dependent frequencies during resonant interactions [13]. This phenomenon can be exploited in the domain of noise mitigation, for instance, by employing Helmholtz resonators in nonlinear domains [15–19] to establish a TET between an acoustic mode and the resonator [20]. Geometric nonlinearities exhibited for instance by visco-elastic membranes have also been used in vibro-acoustics to trigger acoustical modes [21–23]. Beyond pure cubic nonlinearities, other types of nonlinearities have also been exploited for mechanical systems [24, 25], such as vibro-impact [26–28], piece-wise linear and hybrid nonlinear-linear [29–31], and time-dependent [32]. TET has also been studied in the context of systems with time-dependent physical and mechanical properties such as time-varying masses [33]. One of the methods for designing the TET is the identification of the Slow Invariant Manifold (SIM) [34, 35] and characteristic points of the system such as equilibrium points and singularities [36]. The SIM is mostly a critical manifold of singularity perturbed fast-slow governing equations [37]. The perturbation is introduced using a small physical perturbation parameter representing the (modal) mass ratio between the oscillators which perform the TET. One of the challenges in designing a NES is the tuning of its activation threshold to leverage the nonlinearity and trigger a TET. Recently, several studies have been conducted to improve the effectiveness of NES by changing the activation threshold. Examples of studies include bistable NESs [38–40], beams with acoustic black hole [41, 42], and

specific geometries [43]. Depending on the initial conditions and other system parameters such as the external excitation one or several bifurcations can occur. However, it is well known that the NES efficiency is very sensitive to perturbations of the systems parameters or loading conditions [44]. In fact, this sensitivity is such that it can lead to discontinuous responses, switching abruptly, for instance, from high to low NES efficiencies. For these reasons, optimizing the NES design while accounting for uncertainties is essential. The system under consideration in this paper is composed of a linear oscillator, which is linearly and weakly coupled to a NES with a time-dependent cubic nonlinearity. A stochastic optimization technique [45] based on developments by Boroson and Missoum [46] is used to account for different sources of uncertainties in the design of the NES with time-dependent nonlinearity. The optimization scheme is based on a Gaussian Process surrogate to significantly reduce the computational burden **and can also tackle potential discontinuities exhibited by the system**. The time-dependent nonlinear resonator, its **robust design** optimization with a dedicated approach, and the comparison with a constant cubic nonlinear absorber constitute the main novelties of this article.

Note that the use of variable stiffness can be found in several engineering applications. In [47], the authors exploited variable-stiffness electromagnetic actuators able to perform adaptive shape morphing and latching of a multiple degrees of freedom robotic finger. Other applications involve the programming electro-acoustic resonators [48] to impose desired nonlinear stiffnesses: Duffing-type [49], non-polynomial [50], and time-dependent cubic non-linearities (as done in this work) [32] to control acoustical mode(s).

The article is organized as follows: Section 2 presents the system as well as analytical developments to characterize its various dynamics. The Section also demonstrates the effects of uncertainties on the system's responses. Section 3 describes the stochastic optimization problem along with the solution techniques. In Section 4, the optimization approach is applied to NES with a time-dependent cubic nonlinearity and compared to the case of optimized constant nonlinearity. Results are discussed in Section 5. Finally, conclusions and perspectives are provided in Section 6.

## 2. Two-degree of freedom system with time-varying nonlinearity

This section introduces the system used in this study. Its fast and slow dynamics are investigated through analytical developments. Metrics to quantify

the behavior of the system for optimization purposes are also presented.

### 2.1. Presentation of system

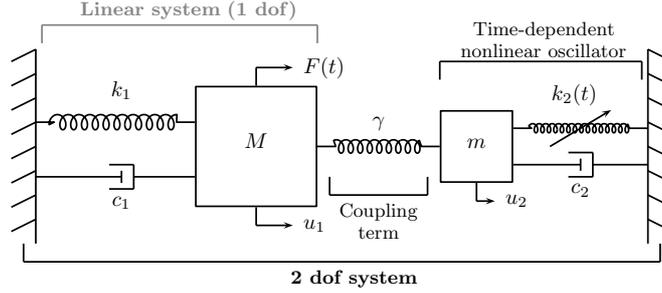


Figure 1: Academic representation of the studied system.

In this study, we are considering a two degree-of-freedom (dof) system consisting of a primary linear system linearly coupled to a nonlinear absorber (Fig. 1). It has been extensively studied in [32]. The main system has a mass  $M$ , a damping  $c_1$ , and a stiffness  $k_1$ . The nonlinear system consists of a mass  $m$ , a time-dependent nonlinear stiffness  $k_2(t)$ , and a damping  $c_2$ . The coupling stiffness is  $\gamma$ . The displacements of the masses  $M$  and  $m$  are denoted as  $u_1$  and  $u_2$ , respectively. The main mass  $M$  is subjected to an external force  $F(t) = F_0 \sin(\Omega t)$ . The governing equations of the system are as follows:

$$\begin{cases} M \frac{\partial^2 u_1}{\partial t^2} + k_1 u_1 + c_1 \frac{\partial u_1}{\partial t} + \gamma(u_1 - u_2) = F_0 \sin(\Omega t) \\ m \frac{\partial^2 u_2}{\partial t^2} + c_2 \frac{\partial u_2}{\partial t} + \gamma(u_2 - u_1) + k_2(t) u_2^3 = 0 \end{cases} \quad (1)$$

We introduce a dimensionless time  $\tau = \sqrt{\frac{k_1}{M}} t = \omega_1 t$  and a mass ratio  $\varepsilon$  such as  $0 < \varepsilon = \frac{m}{M} \ll 1$ . With these new variables, Eq. (1) becomes:

$$\begin{cases} \frac{\partial^2 u_1}{\partial \tau^2} + u_1 + \varepsilon \xi_1 \frac{\partial u_1}{\partial \tau} + \varepsilon \gamma_0 (u_1 - u_2) = \varepsilon f \sin(\nu \tau) \\ \varepsilon \frac{\partial^2 u_2}{\partial \tau^2} + \varepsilon \xi_2 \frac{\partial u_2}{\partial \tau} + \varepsilon \gamma_0 (u_2 - u_1) + \varepsilon k(\tau) u_2^3 = 0 \end{cases} \quad (2)$$

with  $\varepsilon\xi_1 = \frac{c_1}{\sqrt{k_1}M}$ ,  $\varepsilon\xi_2 = \frac{c_2}{\sqrt{k_1}M}$ ,  $\varepsilon\gamma_0 = \frac{\gamma}{k_1}$ ,  $\varepsilon k(\tau) = \frac{k_2(t)}{k_1}$ ,  $\varepsilon f = \frac{F_0}{k_1}$ , and  $\nu = \frac{\Omega}{\omega_1}$ . To study the system around the 1:1 resonance, we define  $\nu = 1 + \sigma\varepsilon$  where  $\sigma$  is denoted as detuning parameter.

We assume that the time-dependent stiffness varies around a constant value and can be represented by a Fourier series:

$$k(\tau) = \sum_{n=-\infty}^{+\infty} K_n e^{in\nu\tau} \quad (3)$$

where  $K_{-n} = K_n^*$  and  $(*)$  stands for the complex conjugate.

## 2.2. Analytical study to identify the various dynamics

The system can be analytically studied to predict its behavior with respect to parameters, external excitation, and initial conditions. The method is described in detail by Labetoulle et al. [32]. First, the complex variables of Manevitch [51, 52], corresponding to the envelope of the system response, are introduced:

$$\varphi_m e^{i\nu\tau} = \dot{u}_m + i\nu u_m \quad (4)$$

where  $m = 1, 2$  and  $(\dot{\cdot})$  stands for the derivative with respect to  $\tau$ . The complex variables can be expressed in polar coordinates as follows:

$$\varphi_m = N_m e^{i\delta_m} \quad (5)$$

Then, a multiple scale method [53] is used and different time scales are introduced: a fast time scale  $\tau_0 = \tau$  and slow time scales  $\tau_j = \varepsilon^j \tau$  ( $j = 1, 2, \dots$ ). Afterward, only the first harmonic is retained using the Galerkin method. By denoting  $\dot{\varphi}$  as the derivative of  $\varphi$  with respect to  $\tau$ , Eq. (2) becomes:

$$\begin{cases} \dot{\varphi}_1 + \frac{i}{2}\nu\varphi_1 + \frac{1}{2}\varepsilon\xi_1\varphi_1 + \frac{1}{2i\nu}\varphi_1 + \varepsilon\gamma_0\frac{1}{2i\nu}(\varphi_1 - \varphi_2) = \frac{\varepsilon f}{2i} \\ \varepsilon(\dot{\varphi}_2 + \frac{i}{2}\nu\varphi_2) + \frac{1}{2}\varepsilon\xi_2\varphi_2 + \varepsilon\gamma_0\frac{1}{2i\nu}(\varphi_2 - \varphi_1) \\ \quad + \frac{\varepsilon i}{8\nu^3}(\varphi_2^3 K_{-2} - 3K_0|\varphi_2|^2\varphi_2 + 3K_2|\varphi_2|^2\varphi_2^* - \varphi_2^{*3}K_4) = 0 \end{cases} \quad (6)$$

So, after keeping the first harmonic of the restoring force  $k(\tau)u_2^3$ , considering  $K_0 \in \mathbb{R}$  and  $K_n = k_{nr} + ik_{ni}$ , only the terms corresponding to  $n = 2$  and  $n = 4$  are retained in Eq. 3. The time-dependent stiffness reads:

$$k(\tau) = k_0 + 2k_{2r} \cos(2\nu\tau) - 2k_{2i} \sin(2\nu\tau) + k_{4r} \cos(4\nu\tau) - k_{4i} \sin(4\nu\tau) \quad (7)$$

The study of Eq. (6) at the order  $\varepsilon^0$ , which corresponds to the fast dynamics, yields the equation of the Slow Invariant Manifold (SIM), noted as  $\mathcal{H}$ , defined as:

$$\frac{\partial \varphi_2}{\partial \tau_0} - \frac{1}{2} \underbrace{\left( \varphi_2(2i + \xi_2 - i\gamma_0) + i\gamma_0\varphi_1 - \frac{i\varphi_2}{4} \left( \varphi_2^2 K_2^* - 3|\varphi_2|K_0 + 3\varphi_2^{*2} K_2 - \varphi_2^{*4} K_4 \right) \right)}_{\mathcal{H}} = 0 \quad (8)$$

We are looking for an asymptotic state as  $\tau_0$  tends to  $\infty$ , leading to  $\mathcal{H} = 0$  and:

$$N_1 = \frac{N_2}{\gamma_0} \sqrt{A(N_2, \delta_2)^2 + B(N_2, \delta_2)^2} \quad (9)$$

where  $A$  and  $B$  are detailed in Appendix A. We can notice that for a more classical case with a constant nonlinearity ( $k(\tau) = k_0$ ), the SIM is independent of the phase  $\delta_2$ . The boundary of the unstable zone of the SIM (Eq. (10)) can be detected by introducing a perturbation of  $\varphi_2$  in Eq. (8), leading to the following polynomial equation:

$$a_v N_2^4 + b_v N_2^2 + c_v = 0 \quad (10)$$

where  $a_v$ ,  $b_v$ , and  $c_v$  are detailed in Appendix B.

Equation (6) is examined at the order  $\varepsilon^1$ , representing the slow dynamic, to detect equilibrium and singular points. The equation for equilibrium points can be derived from the first equation of Eq. (6) at the order  $\varepsilon^1$  by setting  $\mathcal{E} = 0$ , where  $\mathcal{E}$  is defined as:

$$\frac{\partial \varphi_1}{\partial \tau_1} + \frac{1}{2} \underbrace{(2i\sigma\varphi_1 + \xi_1\varphi_1 - i\gamma_0(\varphi_1 - \varphi_2) - if)}_{\mathcal{E}} = 0 \quad (11)$$

Then, the equation of equilibrium points is:

$$p_{10}N_2^{10} + p_8N_2^8 + p_7N_2^7 + p_6N_2^6 + p_5N_2^5 + p_4N_2^4 + p_3N_2^3 + p_2N_2^2 + p_0 = 0 \quad (12)$$

where  $p_g$  ( $g = 0, \dots, 10$ ) are defined as a function of  $\sigma$ ,  $f$ ,  $\gamma_0$ ,  $\xi_1$ ,  $\xi_2$ ,  $k_0$ ,  $k_{2r}$ ,  $k_{2i}$ ,  $k_{4r}$ ,  $k_{4i}$ ,  $\delta_2$ , and detailed in Appendix F in [32]. According to [32], the equation of the singular points is the same as the boundaries of the unstable zone and depends on  $\sigma$  (the detuning parameter),  $N_1$ ,  $N_2$ , and  $\delta_2$  (for the variable nonlinearity). In the case of a constant nonlinearity ( $k(\tau) = k_0$ ), the equation of equilibrium points is simpler and is given by:

$$p_{6,c}N_2^6 + p_{4,c}N_2^4 + p_{2,c}N_2^2 + p_{0,c} = 0 \quad (13)$$

with

$$\begin{cases} p_{6,c} = \left(\frac{3}{4}k_0\right)^2 [\xi_1^2 + (2\sigma - \gamma_0)^2] \\ p_{4,c} = \frac{3}{2}k_0 [(-1 + \gamma_0) [\xi_1^2 + (2\sigma - \gamma_0)^2] + (2\sigma - \gamma_0)\gamma_0^2] \\ p_{2,c} = (-1 + \gamma_0)^2 [\xi_1^2 + (2\sigma - \gamma_0)^2] + 2(-1 + \gamma_0)(2\sigma - \gamma_0)\gamma_0^2 \\ \quad + (\xi_1\xi_2 + \gamma_0^2)^2 + (2\sigma - \gamma_0)^2\xi_2^2 \\ p_{0,c} = -f^2\gamma_0^2 \end{cases} \quad (14)$$

Different dynamics of the forced system can be predicted by examining the equilibrium points. Depending on the parameters, the external force, and the initial conditions, the system can exhibit periodic or quasi-periodic regimes. Figure 2 illustrates the equilibrium points for various cases. Specifically, Figs. 2a, 2b, and 2c correspond to a system with a constant nonlinearity ( $k(\tau) = k_0$ ) while Fig. 2d represents a system with variable stiffness. In each figure, the gray solid, black dotted, and black solid lines represent the equilibrium points of the 2 dof system, the single dof linear system, and the unstable zone of the SIM, respectively.

In the following analysis, only the response of the main system will be considered. Thus, the focus will be on the equilibrium points as functions of  $N_1$  and  $\sigma$ . For cases with constant nonlinearity, the equilibrium points exhibit different behaviors. For example, for relatively small values of  $f$  and  $k_0$ , the equilibrium points present a single branch as shown in Fig. 2a. As  $k_0$  or  $f$  increases, an isolated branch appears in addition to the main branch, corresponding to higher energy levels of the main system (Fig. 2b). The

Parameter	$\varepsilon$	$\xi_1$	$\xi_2$	$\gamma$
Value	0.01	0.1	0.1	0.5

Table 1: Parameters of the 2 dof system

two branches eventually converge (Fig. 2c) as these parameters are further increased. For the system with time-dependent nonlinearity, only one example is given in Fig. 2d with two branches, but the system exhibits similar behaviors to the system with constant nonlinearity. In this case, the graph is more complex due to the dependence of the phase  $\delta_2$ . The solid black line representing the unstable zone of the SIM corresponds to a quasi-periodic regime [54].

### 2.3. Examples of dynamic behaviors: discontinuities, periodicity, and quasi-periodicity

To study the various dynamical behaviors of the system, numerical results are provided for both constant and variable stiffnesses. The results are also compared to analytical predictions reported in Fig. 2. The simulations are carried out with the parameters presented in Table 1 under initial conditions set to zero for all variables, i.e.  $(u_1(\tau = 0), u_2(\tau = 0), \dot{u}_1(\tau = 0), \dot{u}_2(\tau = 0)) = (0, 0, 0, 0)$ . Equation (2) is numerically integrated using the Runge-Kutta method, implemented with the MATLAB function “ode45”. The displacements and velocities  $u_m(\tau)$  and  $\dot{u}_m(\tau)$  are used to compute the amplitudes  $N_m = \sqrt{\dot{u}_m(\tau)^2 + (\nu u_m(\tau))^2}$ ,  $m = 1, 2$  (Eqs. (4) and (5)). Figure 3 depicts the numerical results for the system with constant nonlinearity ( $k_0 = 0.7$ ,  $f = 0.4$ ), while Fig. 4 shows the numerical results for the system with variable stiffness ( $k_0 = 0.5$ ,  $k_{2r} = 0.1$ ,  $k_{2i} = k_{4r} = k_{4i} = 0$ , see Eq. 3, and  $f = 0.3$ ). The responses of the 2 dof system are represented by solid gray lines and those of the single dof system by dotted black lines. Figures 3a and 3b illustrate the variations of  $N_1(\tau)$  and  $N_2(\tau)$  for  $\sigma = -0.15$  demonstrating that the 2 dof system is in periodic regime and on the isola (Fig. 2b). Meanwhile, Fig. 3c represents the time response of  $N_1(\tau)$  for  $\sigma = -0.25$  where the 2 dof system is also in a periodic regime but on the main branch of the equilibrium point, corresponding to a lower energy level (Fig. 2b). Figures 4a and 4b depict  $N_1(\tau)$  and  $N_2(\tau)$  for  $\sigma = 0.88$  while Fig. 4c corresponds to  $N_1(\tau)$  for  $\sigma = 0.89$ . In Figs. 4a and 4b, the 2 dof system is in quasi-periodic regime ( $\sigma$  is in the unstable zone of the SIM see Fig. 2d), while in Fig. 4c, the

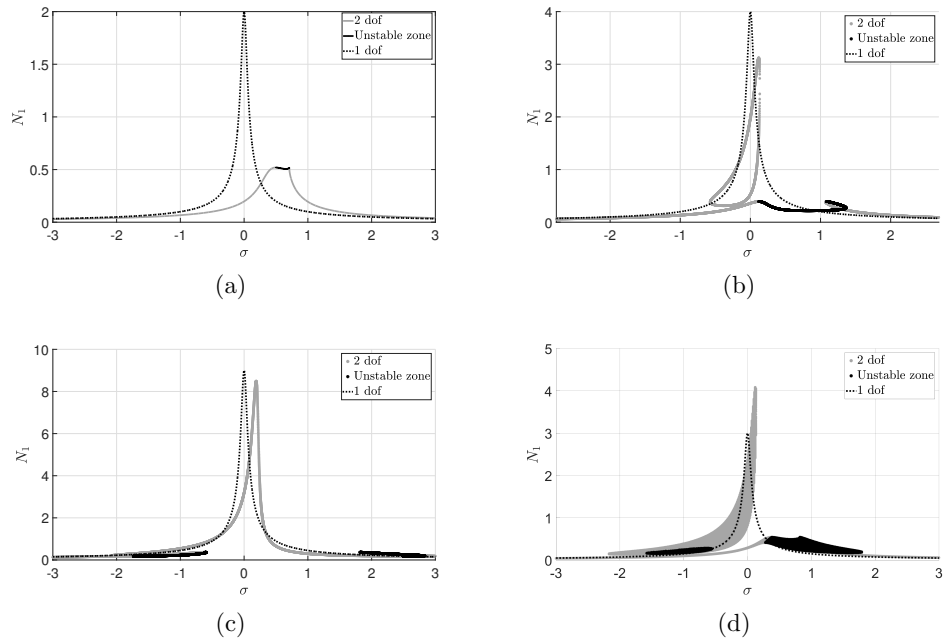


Figure 2: Equilibrium points of 1 dof (without coupled nonlinear absorber) and 2 dof (with coupled absorber) systems with respect to  $N_1$  versus the detuning parameter  $\sigma$  for several sets of parameters: a)  $f = 0.2$ ,  $k_0 = 0.4$  (constant nonlinearity); b)  $f = 0.4$ ,  $k_0 = 0.7$  (constant nonlinearity); c)  $f = 0.9$ ,  $k_0 = 0.8$  (constant nonlinearity); d)  $f = 0.3$ ,  $k_0 = 0.5$ ,  $k_{2r} = 0.1$  (time-variable nonlinearity). The specific parameter values are detailed in Table 1.

system is on the main branch in a periodic regime. As a summary, the results presented in Figs. 3 and 4 illustrate the possibility of existence of periodic and quasi-periodic regimes. Furthermore, the system can be attracted by an equilibrium point located on the main branch of the frequency response curve, corresponding to lower energy amplitudes for the main mass, or by a point located on the isola, representing higher energies of the main system.

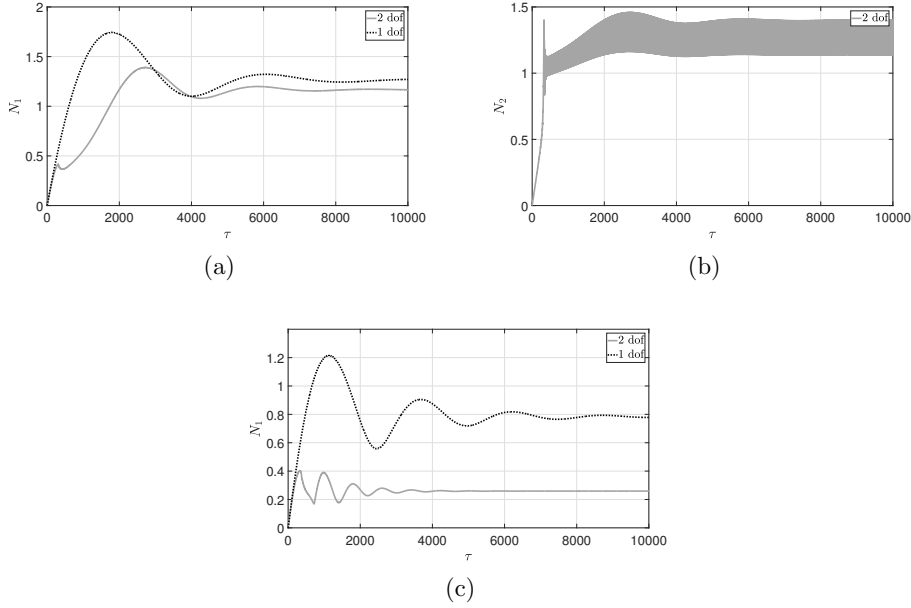


Figure 3: Main system amplitude ( $N_1(\tau)$ ) in the case of a 2 dof (solid gray curve) and 1 dof (dotted black curve) system and absorber amplitude ( $N_2(\tau)$ ) (solid gray curve), for different values of the detuning parameter  $\sigma$ . a)  $N_1(\tau)$  for  $\sigma = -0.15$ ; b)  $N_2(\tau)$  for  $\sigma = -0.15$ ; c)  $N_1(\tau)$  for  $\sigma = -0.25$  with  $k_0 = 0.7$ ,  $f = 0.4$ , and parameters detailed in Table 1. The results are obtained from direct numerical integration of Eq. (2) for initial conditions as:  $(u_1(\tau = 0), u_2(\tau = 0), \dot{u}_1(\tau = 0), \dot{u}_2(\tau = 0)) = (0, 0, 0, 0)$ .

It is interesting to note that for specific parameter values, as predicted by the equilibrium points, the amplitude of the response of the main system with NES is higher than the one without NES (Fig. 4c). Additionally, the isola, although corresponding to an important energy level, does not necessarily end to a higher amplitude response than without the coupled NES (Fig. 3a).

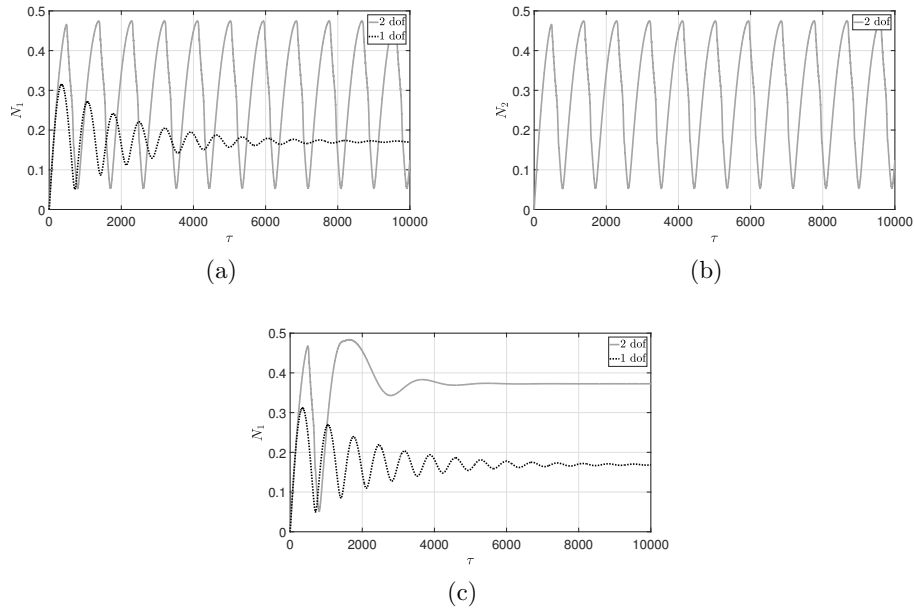


Figure 4: Main system amplitude ( $N_1(\tau)$ ) in the case of a 2 dof (solid gray curve) and 1 dof (dotted black curve) system and absorber amplitude ( $N_2(\tau)$ ) (solid gray curve), for different values of the detuning parameter  $\sigma$ . a)  $N_1(\tau)$  for  $\sigma = 0.88$ ; b)  $N_2(\tau)$  for  $\sigma = 0.88$ ; c)  $N_1(\tau)$  for  $\sigma = 0.89$  with  $k_0 = 0.5$ ,  $k_{2r} = 0.1$ ,  $f = 0.4$ , and parameters detailed in Table 1. The results are obtained from direct numerical integration of Eq. (2) for initial conditions as:  $(u_1(\tau = 0), u_2(\tau = 0), \dot{u}_1(\tau = 0), \dot{u}_2(\tau = 0)) = (0, 0, 0, 0)$ .

These observations emphasize the complex interplay of system parameters and their influence on the behavior of the system.

Moreover Fig. 3 reveals two very different response amplitudes for closely spaced values of  $\sigma$ . This indicates the presence of discontinuous behavior with respect to system parameters such as  $\sigma$  and the nonlinear stiffness. Such discontinuity is also visible for a slight variation of the stiffness ( $k_0$ ) which significantly affects the amplitude of the response of the main system. This is demonstrated in Fig. 5 where the black dotted curve corresponds to the response of the single dof system for  $\sigma = -0.2$  and  $f = 0.4$ . Subsequently, the gray solid and gray dashed curves represent the response of the main system with NES for  $k_0 = 0.65$  and  $k_0 = 0.7$ , respectively. It can be observed that for the system with  $k_0 = 0.7$ , the response is approximately equal to 1 in a stationary regime, as for the single dof system, while for the system with  $k_0 = 0.65$ , the response is approximately 0.3.

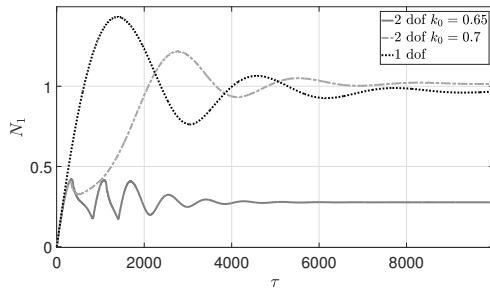


Figure 5: Time responses of  $N_1(\tau)$  corresponding to the 2 dof and 1 dof systems for  $k_0$  values close to each other showing large differences in amplitudes during the stationary regimes. The values of  $k_0$  are:  $k_0 = 0.65$  (gray solid line),  $k_0 = 0.7$  (gray dashed line) and without NES (black dotted line) ( $\sigma = -0.2$ ,  $f = 0.4$ , and parameters in Table 1). The results are obtained from direct numerical integration of Eq. 2 for initial conditions as:  $(u_1(\tau = 0), u_2(\tau = 0), \dot{u}_1(\tau = 0), \dot{u}_2(\tau = 0)) = (0, 0, 0, 0)$ .

These discontinuities demonstrate that the NES is highly sensitive to uncertainties, which play a crucial role in the dynamics and efficiency of the NES [44, 55]. The NES efficiency is particularly sensitive to slight perturbations of the design parameters and external excitation [56]. In many cases, the optimization process to maximize vibration absorption might locate the optimal solution on the boundary between high and low efficiency regions, leading to a design whose performance can vary drastically with small perturbations in

the design parameters and/or external force [44].

In the next subsection, an efficiency metric of the NES is presented along with some deterministic optimization results.

#### 2.4. Efficiency metric

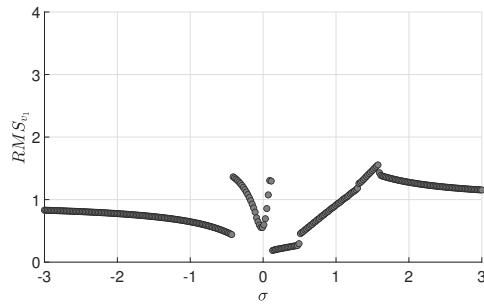
Various approaches exist to characterize the efficiency of NES. For instance, previous works have investigated the NES optimization by computing the energy dissipated by the NES coupled to a system subjected to an initial velocity [44, 46]. In the present study, we consider a linear system subjected to a forced excitation. The NES efficiency is quantified by comparing the responses of the system with and without the NES. Specifically, we chose the root mean square (RMS) value of the time response of the velocity of the main mass,  $\dot{u}_1(\tau)$  taking into account the response of the main system in both transient regime and steady state, which is relevant for forced excitation. The RMS response is obtained by numerical integration of Eq. 2. The metric is defined as follows:

$$RMS_{v_1} = \frac{RMS_{2dof}(\dot{u}_1(\tau))}{RMS_{1dof}(\dot{u}_1(\tau))} \quad (15)$$

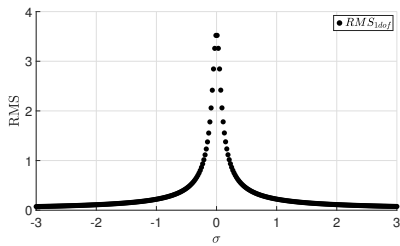
where  $RMS_{2dof}(\dot{u}_1(\tau))$  is the RMS of the velocity of the main mass  $M$  of the 2 dof system with NES, and  $RMS_{1dof}(\dot{u}_1(\tau))$  is the RMS of the linear main system velocity without NES.

The integration time is a crucial parameter. It should be long enough to allow systems to reach their stationary or quasi-periodic regimes. For the 2 dof system, it strongly depends on the parameter  $\varepsilon$ : a smaller value demands a longer integration time to reach to stationary regimes [57]. To obtain an acceptable integration time and to facilitate the optimization, the mass ratio is set to  $\varepsilon = 0.01$ .

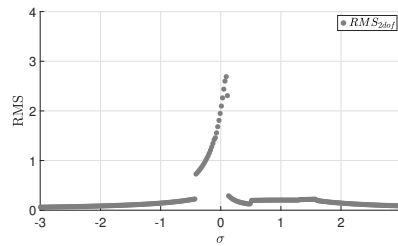
The discontinuities highlighted in the previous sub-section are also present with this metric. Figures 6a, 6b, and 6c represent  $RMS_{v_1}$ ,  $RMS_{1dof}$ , and  $RMS_{2dof}$  as functions of  $\sigma$ , respectively, for  $\sigma \in [-3; 3]$ ,  $k_0 = 0.7$ ,  $k_{2r} = 0.2$ ,  $f = 0.6$ , and parameters presented in Table 1. Two major discontinuities are visible: the first one for  $\sigma \in [-0.3; 0.1]$  corresponds to the isola and the second one for  $\sigma \in [0.1; 0.5]$  corresponds to the unstable branch of the SIM and to a quasi-periodic regime.



(a)



(b)



(c)

Figure 6: Root mean square (RMS) as a function of  $\sigma \in [-3; 3]$ . a)  $RMS_{v_1}$ ; b)  $RMS_{1dof}$ ; c)  $RMS_{2dof}$ . System parameters are:  $k_0 = 0.7$ ,  $k_{2r} = 0.2$ ,  $f = 0.6$ , and those reported in Table 1. We note that discontinuities exist near resonance.

### 2.5. Deterministic optimization

In this section, we present results for the deterministic optimization of the NES stiffness without considering uncertainties. These results are given as a reference for the stochastic optimization of the following sections.

For given characteristics of the external force such as the amplitude  $f$  and the detuning parameter  $\sigma$ , we search for the constant and variable nonlinear stiffness parameters ( $k_0$  and  $k_0, k_{2r}$ , respectively) that minimize  $RMS_{v_1}$ . A Particle Swarm Optimization (PSO) method [58], which is a zero-order global optimization approach, is used. PSO is insensitive to discontinuities and is therefore suitable for this deterministic optimization. The bounds of the design variable parameters are:  $k_0 \in [0.1; 1]$ ,  $k_{2r} \in [0; 0.5]$  and those of the aleatory variables are:  $\sigma \in [-2; 2]$ ,  $f \in [0.3; 0.7]$ .

Figure 7 depicts the deterministic optimization of the system with constant nonlinearity ( $k = k_0$ ). More precisely, Fig. 7a corresponds to the optimal stiffness ( $k_{0,opt}$ ) and Fig. 7b shows the objective function  $RMS_{v_1}$  for  $k_{0,opt}$ , named  $RMS_{v_1,opt}$ , as functions of  $\sigma$  and  $f$ . We observe that the optimization at the resonance level ( $\sigma = 0$ ) is highly dependent on  $\sigma$ .

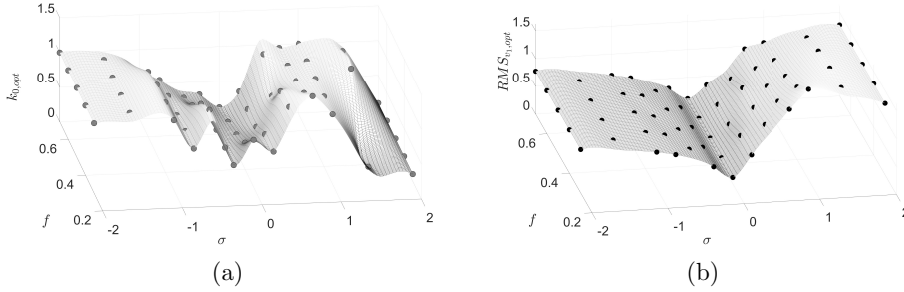


Figure 7: Deterministic optimization for the system with constant nonlinearity ( $k = k_0$ ). a) Optimal  $k_0$ ; b) Optimal  $RMS_{v_1}$  as function of  $\sigma$  and  $f$  with the parameters of Table 1.

In the next section, the stochastic optimization problem and methods will be presented.

### 3. Stochastic Optimization Method

#### 3.1. Optimization Problem Formulation

We would like to maximize the efficiency of the NES for ranges of external excitations considered as random parameters. The optimization problem is formulated as follows:

$$\begin{aligned} \text{Min}_{\mathbf{x}_d} \mathbb{E}_{\mathbf{x}_a} (RMS_{v_1}(\mathbf{x}_d, \mathbf{x}_a)) \\ \text{s.t. } \mathbf{x}_d^{min} \leq \mathbf{x}_d \leq \mathbf{x}_d^{max} \end{aligned} \quad (16)$$

where  $\mathbb{E}$  is the expected value,  $\mathbf{x}_d$  is the vector (deterministic) of design variables,  $\mathbf{x}_d^{min}$  and  $\mathbf{x}_d^{max}$  are the lower and upper bounds.  $\mathbf{x}_a$  is the vector of aleatory variables. The design variables considered in this study are the stiffness parameters of the NES:  $k_0, k_{2r}, k_{2i}, k_{4r}, k_{4i}$  (Eq. 3). The aleatory variables are the amplitude  $f$  and the detuning parameter  $\sigma$  linked to the frequency of the external force.

In order to solve this optimization problem in a tractable way, special techniques are used to reduce the computational cost and handle discontinuities. Specifically, the algorithm splits the space into regions where individual Kriging surrogates can be constructed. The region boundary is defined by a Support Vector Machine (SVM) classifier based on the results of a clustering algorithm. Finally, an adaptive sampling scheme is used to iteratively refine the Kriging surrogates and the region boundary. The following subsections describe the main components of the stochastic optimization approach and the corresponding algorithm.

#### 3.2. Clustering

As shown in Sect. 2.3, the response of the 2 dof system exhibits discontinuities and strong gradients, due to the presence of isolas and unstable zones. Several clusters are visible in Fig. 6, demonstrating the complex dynamics of the system. Figure 6a reveals several discontinuities: the upper branch for  $\sigma \in [-0.5; 0]$  corresponds to the isola, and the lower one around  $\sigma = 0.3$  is due to the quasi-periodic regime. The complexity of the problem increases with the dimensionality (i.e., the number of variables and parameters). In this paper, we choose to divide the dynamic responses into two classes, loosely corresponding to two levels of efficiency. These clusters can be identified in an unsupervised manner using techniques such as K-means [59].

### 3.3. Support Vector Machine (SVM) boundary

Following the unsupervised clustering into two classes, a SVM classifier [60–62] is used to identify the boundary of the regions in the design and aleatory variables space by handling discontinuities. SVM provides an explicit expression of the boundary in terms of the parameters. Given a set of  $N$  training samples  $x_i$  in a  $d$ -dimensional space and the corresponding class label  $y_i$ , the SVM boundary is written as:

$$s(\mathbf{x}) = b + \sum_{i=1}^N \lambda_i y_i K(x_i, \mathbf{x}) = 0 \quad (17)$$

where  $b$  is a scalar called the bias,  $\lambda_i$  are Lagrange multipliers obtained from the quadratic programming optimization problem used to construct the SVM boundary, and  $K$  is a kernel function. The classification of any arbitrary point  $\mathbf{x}$  is given by the sign of  $s(\mathbf{x})$ . The training samples for which the Lagrange multipliers are non-zero, are called support vectors. The chosen kernel function  $K$  in Eq. (17) is the Gaussian kernel defined as:

$$K(\mathbf{x}_i, \mathbf{x}_j) = \exp\left(-\frac{\|\mathbf{x}_i - \mathbf{x}_j\|^2}{2\sigma^{*2}}\right) \quad (18)$$

where  $\sigma^*$  is the width parameter. The SVM boundary covers the entire space and will be refined during the optimization process (see Sect. 3.5).

### 3.4. Computation of objective function

Numerical integrations using the Runge-Kutta method can be computationally expensive. Due to the large number of simulations required for optimization and calculation of the expected value, it is not possible to call the ODE solvers directly. Therefore, a Kriging surrogate (also referred to as Gaussian Process) can be employed to obtain an approximation of  $RMS_{v_1}$  for various combinations of the design and aleatory variables [46]. These combinations are obtained through a design of experiments (DOE) such as Latin Hypercube Sampling (LHS).

Based on the clustering and SVM results, two Kriging surrogates are constructed over the two regions. These surrogates correspond to two levels of efficiency. An example with two variables ( $k_0$  and  $\sigma$ ) is presented in Fig. 8. In detail, Fig. 8a depicts an example with two clusters and an SVM boundary. The black crosses represent the cluster with a high response amplitude, while the gray dots represent the cluster with a lower amplitude.

The black line represents the SVM boundary separating the two clusters. Two corresponding Kriging surrogates are shown in Fig. 8b.

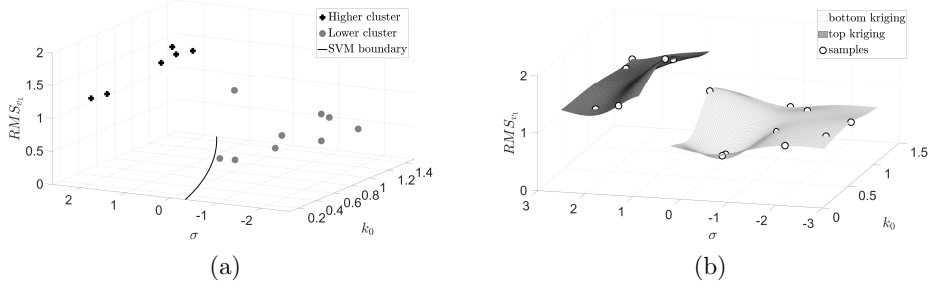


Figure 8: a) Separation of the responses into two clusters and SVM boundary of the two regions; b) Krigings corresponding to the two clusters.

The computation of the expected value is based on Monte Carlo simulations, such as:

$$\mathbb{E}_{\mathbf{X}_a} (RMS_{v_1}(\mathbf{x}_d, \mathbf{x}_a)) \approx \frac{1}{N_{lhs}} \sum_{i=1}^{N_{lhs}} I_s(\mathbf{x}_i) \quad (19)$$

with

$$I_s(\mathbf{x}_i) = \begin{cases} \widetilde{RMS}_{v_1,1}(\mathbf{x}_i) & \text{if } s(\mathbf{x}_i) < 0 \\ \widetilde{RMS}_{v_1,2}(\mathbf{x}_i) & \text{if } s(\mathbf{x}_i) \geq 0 \end{cases} \quad (20)$$

where  $\mathbf{x}_i$  are the Monte Carlo samples following the distributions of  $\mathbf{X}_a$ .  $\widetilde{RMS}_{v_1,1}$  and  $\widetilde{RMS}_{v_1,2}$  are the kriging surrogates based on the two clusters: high and low efficiency samples.  $s(\mathbf{x})$  is the SVM approximation. The sign of  $s(\mathbf{x})$  determines the classes of the samples.  $s(\mathbf{x}) < 0$  means that the sample  $\mathbf{x}$  belongs to the lower efficiency cluster and the corresponding Kriging and vice versa.

### 3.5. Stochastic Optimization Algorithm

The optimization process begins with an initial DOE. At this stage, the Kriging approximations and the SVM boundary are generally imprecise due to the limited number of samples. They are refined iteratively using an adaptive sampling scheme. Two adaptive samples are added per iteration.

First, we search for the optimal stiffness parameters (Eq. (21)). Then, for this stiffness, the component in the aleatory space for which kriging is least accurate are identified (Eq. (22)). This sample is added to refine the Kriging. Finally, the second sample is a variation of the generalized max-min sampling scheme [63] and is dedicated to the refinement of the SVM boundary (Eq. (23)) [64]. The entire optimization algorithm can be summarized as follows:

- (a) Construct the Design of experiments (DOE) in the  $(\{\mathbf{x}_d, \mathbf{X}_a\})$  space. Compute  $RMS_{v_1}$  for each sample.
- (b) Divide samples into two groups using unsupervised clustering based on the  $RMS_{v_1}$  values.
- (c) Construct an SVM trained from the class labels from the two clusters. The SVM is the boundary between two regions associated with distinct system RMS responses.
- (d) Construct a Kriging approximation over the two regions identified by clustering and SVM.
- (e) Solve an approximation of the optimization problem at the  $n^{\text{th}}$  iteration. The solution is performed using a global optimizer such as Particle Swarm Optimization (PSO) which is efficiently run using the Kriging surrogates.

$$\begin{aligned} \mathbf{x}_d^{(n)} = \arg \min_{\mathbf{x}_d} \quad & \mathbb{E}_{\mathbf{X}_a} \left( \widetilde{RMS}_{v_1}(\mathbf{x}_d, \mathbf{x}_a) \right) \\ \text{s.t.} \quad & \mathbf{x}_d^{\min} \leq \mathbf{x}_d \leq \mathbf{x}_d^{\max} \end{aligned} \quad (21)$$

- (f) Find the aleatory component  $\mathbf{x}_a^{(n)}$  that maximizes the Kriging variance for  $\mathbf{x}_d^{(n)}$  with PSO. Add  $RMS_{v_1}(\mathbf{x}_d^{(n)}, \mathbf{X}_a^{(n)})$  to the samples.

$$\begin{aligned} \mathbf{x}_a^{(n)} = \arg \max_{\mathbf{x}_a} \quad & f_{\mathbf{x}_a}(\mathbf{x}_a)^{\frac{1}{N_a}} \hat{\sigma}^2(\mathbf{x}_a) \\ \text{s.t.} \quad & \mathbf{x}_a^{\min} \leq \mathbf{x}_a \leq \mathbf{x}_a^{\max} \end{aligned} \quad (22)$$

with  $f_{\mathbf{x}_a}$  the joint density function of  $\mathbf{x}_a$  at  $\mathbf{x}_d^{(n)}$ ;  $N_a$  the number of random parameters;  $\hat{\sigma}^2$  the variance of the Kriging;  $\mathbf{x}_a^{\min}$  and  $\mathbf{x}_a^{\max}$  the limits of random parameters.

(g) Refine the SVM boundary using a max-min sampling:

$$\begin{aligned} \mathbf{x}_{\text{mm}} = \arg \max_{\mathbf{x}} \min_i \|\mathbf{x} - \mathbf{x}^{(i)}\| \\ \text{s.t. } s(x) = 0 \\ \mathbf{x}^{\text{min}} \leq \mathbf{x} \leq \mathbf{x}^{\text{max}} \end{aligned} \quad (23)$$

where  $\mathbf{x}^{(i)}$  represents the  $i^{\text{th}}$  existing samples used to train the SVM  $s$  (Eq. 17).

(h) Update the SVM and the Krigings. Repeat steps (e) to (g) until  $\mathbb{E}_{\mathbf{x}_a}(\widetilde{RMS}_{v_1})$  and  $\mathbf{x}_d^{(n)}$  converge.

Figure 9 presents a flowchart of the algorithm for better readability. In the following Section, some results for a constant and time-varying non-linearity are provided.

## 4. Results

The optimal design of a NES with time-dependent nonlinearity is investigated. For comparison, the NES optimization with constant stiffness is also carried out.

### 4.1. Optimization problem

For the system with a constant nonlinearity, the optimization problem is formulated as:

$$\begin{aligned} \text{Min}_{k_0} \quad & \mathbb{E}_{\Sigma, F}(RMS_{v_1}(k_0, \sigma, f)) \\ \text{s.t.} \quad & 0.1 \leq k_0 \leq 1.1 \end{aligned} \quad (24)$$

$$\begin{aligned} \Sigma & \sim \mathcal{N}_t(0, 0.33) \\ F & \sim \mathcal{N}_t(0.55, 0.075) \end{aligned} \quad (25)$$

In this paper, only  $k_0$  and  $k_{2r}$  are considered for the time-dependent nonlinearity, and the other stiffness parameters ( $k_{2i}$ ,  $k_{4r}$ , and  $k_{4i}$ , Eq. 3) are equal to zero. Moreover, the variable stiffness should remain positive so the upper bound of  $k_{2r}$  depends on  $k_0$ , and we also impose  $k_{2r} \leq \frac{k_0}{2}$ . The problem is formulated as it follows:

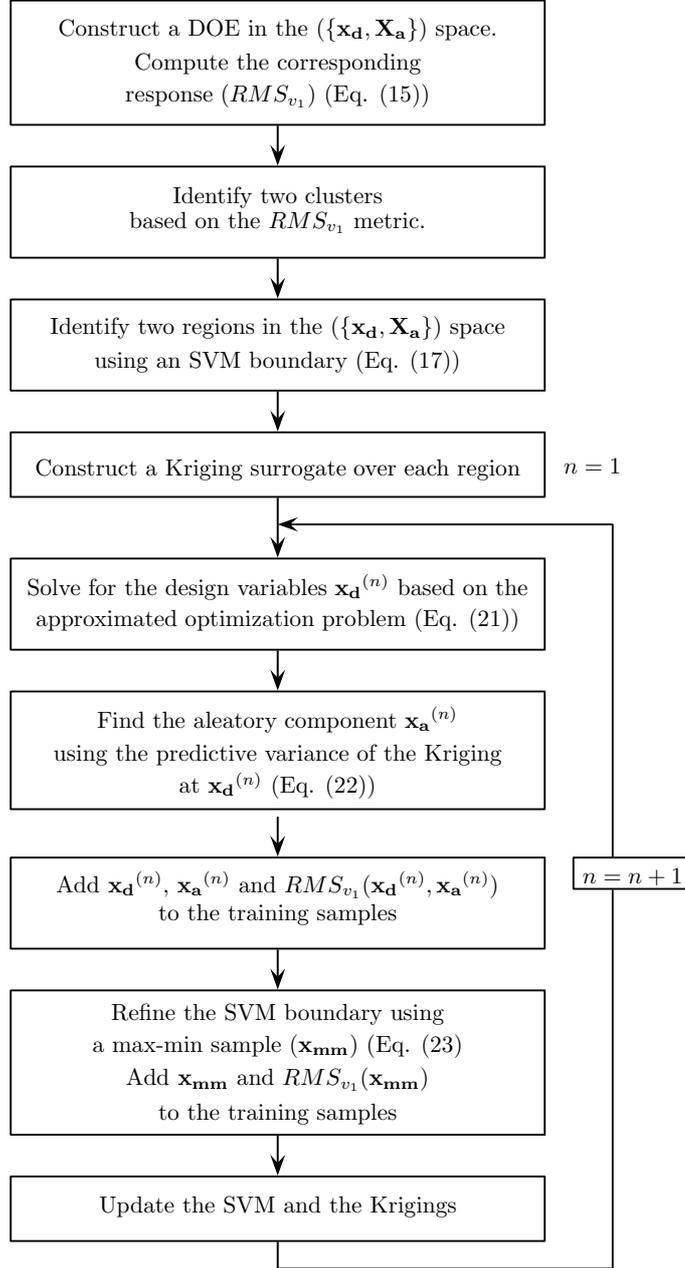


Figure 9: Flowchart of the optimization algorithm.

$$\begin{aligned}
& \underset{k_0, k_{2r}}{\text{Min}} && \mathbb{E}_{\Sigma, F} (RMS_{v_1} (k_0, k_{2r}, \sigma, f)) \\
& \text{s.t.} && 0.1 \leq k_0 \leq 1.1 \\
& && 0 \leq k_{2r} \leq k_0/2
\end{aligned} \tag{26}$$

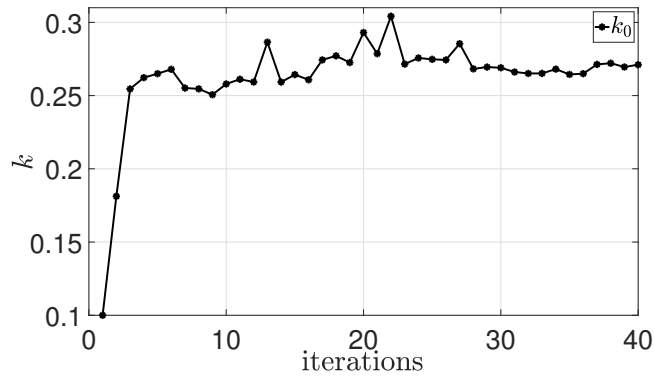
$$\begin{aligned}
& \Sigma \sim \mathcal{N}_t(0, 0.33) \\
& F \sim \mathcal{N}_t(0.55, 0.075)
\end{aligned} \tag{27}$$

where  $\sigma \in [-3; 3]$  and  $f \in [0.1; 1]$  for both cases. The ranges of design and aleatory parameters have been chosen to have the different dynamics of the 2 dof system and to be centered on the resonance of the main linear system. For convenience,  $\mathbb{E}_{\Sigma, F}$  is written as  $\mathbb{E}$ .

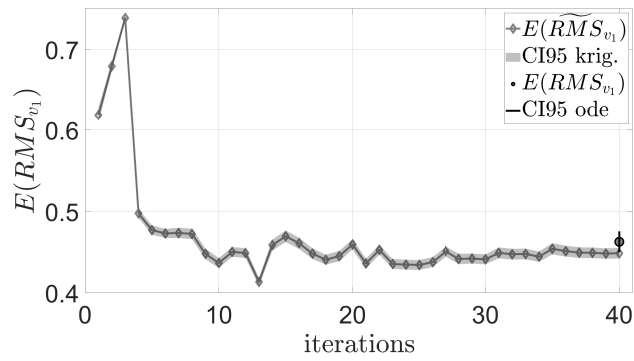
#### 4.2. Results of optimization of the system with constant nonlinearity

For the system with a constant nonlinear stiffness, the optimization is performed with a DOE of 30 samples at the beginning and the computation of  $\mathbb{E} \left( \widetilde{RMS}_{v_1} \left( k_0^{(n)} \right) \right)$  and  $\mathbb{E} (RMS_{v_1} (k_{0,opt}))$  with 4000 and 2000 Monte-Carlo simulations, respectively, where  $k_0^{(n)}$  is the optimal  $k_0$  at the iteration  $n$  and  $k_{0,opt}$  is the optimal  $k_0$  found at the last iteration. Figure 10a corresponds to the evolution of  $k_0^{(n)}$  with respect to the iterations while Fig. 10b represents the evolution of  $\mathbb{E} \left( \widetilde{RMS}_{v_1} \left( k_0^{(n)} \right) \right)$  with respect to the iterations (gray curve with diamonds) with its confidence interval (gray area) and  $\mathbb{E} (RMS_{v_1} (k_{0,opt}))$  for the last iteration (gray dot with black border) with its confidence interval (black solid line). The optimization is considered correct when the two curves ( $k_0^{(n)}$  and  $\mathbb{E} \left( \widetilde{RMS}_{v_1} \left( k_0^{(n)} \right) \right)$ ) converge and when  $\mathbb{E} \left( \widetilde{RMS}_{v_1} \left( k_0^{(n)} \right) \right)$  is close to  $\mathbb{E} \left( RMS_{v_1} \left( k_0^{(n)} \right) \right)$ . Thus, after 40 iterations, we can say that the optimal result is reached. The results of the optimization are presented in Table 2.

In order to understand the behavior at the optimum, the analytically determined equilibrium points for the optimal design are plotted in Fig. 11. In detail, Fig. 11a represents the equilibrium points for four different amplitudes of the external force ( $f = 0.2, f = 0.4, f = 0.6, f = 0.8$ ). In Fig. 11b the equilibrium point for  $f = 0.6$  are isolated for a better readability. Thus, for  $k = k_{0,opt} = 0.271$ , the equilibrium points of 2 dof system present different types of behavior (periodic and quasi-periodic) and an isola is observed for large force amplitudes.



(a)



(b)

Figure 10: Optimization results for the constant case. a) Optimal stiffness at each iteration  $k_0^{(n)}$ ; b)  $\mathbb{E}(\widetilde{RMS}_{v_1}(k_0^{(n)}))$  as a function of iterations. The parameters are detailed in Table 1. The plot indicates convergence after 40 iterations.

$k_{0,opt}$	$\mathbb{E}(\widetilde{RMS}_{v_1})$	$\mathbb{E}(RMS_{v_1})$
0.271	0.449	0.463
CI 95%	[0.442; 0.455]	[0.450; 0.475]
relative error	3.04%	
absolute error	0.014	

Table 2: Results for the constant nonlinearity and the parameters shown in Table 1 after 40 iterations.

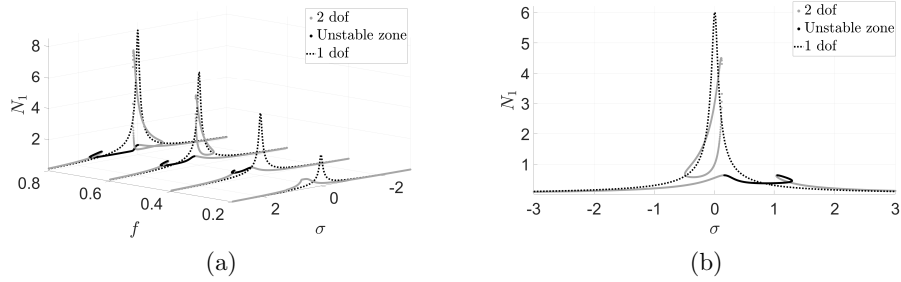


Figure 11: a) Equilibrium points for  $k = k_0 = 0.271$  (optimal stiffness),  $f = 0.2, 0.4, 0.6, 0.8$ ; b) Equilibrium points for  $k = k_0 = 0.271$ ,  $f = 0.6$ , and the parameters in Table 1.

$k_{0,opt}$	$k_{2r,opt}$	$\mathbb{E}(\widetilde{RMS}_{v_1})$	$\mathbb{E}(RMS_{v_1})$
1.041	0.435	0.291	0.298
CI 95%		[0.424; 0.440]	[0.450; 0.466]
relative error	2.37%		
absolute error	0.007		

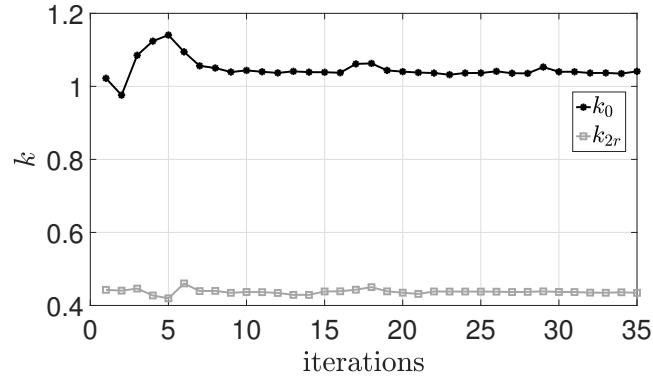
Table 3: Results of the optimization of the time-varying nonlinearity. System parameters are reported in Table 1.

Nevertheless, Figure 11 shows that for the constant stiffness, the amplitude of the equilibrium points of the 2 dof system (gray solid line) remains smaller than that the one of the single dof (black dotted line) under different amplitude of external excitation, i.e.  $f$ , which explains the small value of  $\mathbb{E}(\widetilde{RMS}_{v_1})$ .

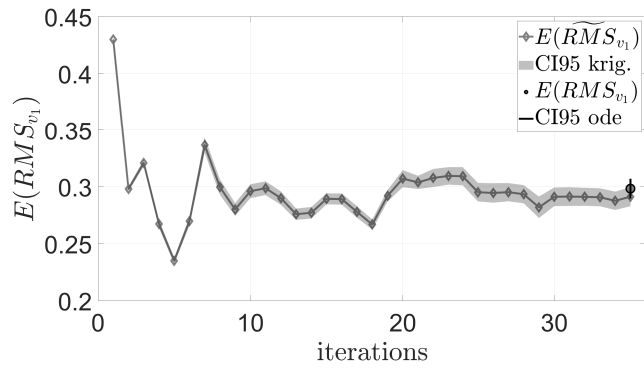
#### 4.3. Results of optimization of the system with time-dependent nonlinearity

To optimize of the time-dependent stiffness, a DOE is initially composed of 40 samples, and the calculation of  $\mathbb{E}(\widetilde{RMS}_{v_1}(k_0^{(n)}, k_{2r}^{(n)}))$  and  $\mathbb{E}(RMS_{v_1}(k_{0,opt}, k_{2r,opt}))$  are performed with 4000 and 2000 Monte Carlo simulations, respectively, where  $k_0^{(n)}$  and  $k_{2r}^{(n)}$  are the optimal parameters of iteration  $n$  and  $k_{0,opt}$  and  $k_{2r,opt}$  are the optimal parameters after the last iteration. The results of the optimization of the time-varying nonlinearity are shown in Fig. 12. In detail, Fig. 12a illustrates  $k_0^{(n)}$  (black curve with crosses) and  $k_{2r}^{(n)}$  (gray curve with squares) as functions of iterations. In Fig. 12b,  $\mathbb{E}(\widetilde{RMS}_{v_1}(k_0^{(n)}, k_{2r}^{(n)}))$  is plotted as a function of iterations with the confidence interval (gray area) and  $\mathbb{E}(RMS_{v_1}(k_{0,opt}, k_{2r,opt}))$  is represented by a gray dot with black border with its confidence interval in black. In Fig. 12a the curves representing  $k_0^{(n)}$  and  $k_{2r}^{(n)}$  as functions of iterations quickly converge, while in Fig. 12b,  $\mathbb{E}(\widetilde{RMS}_{v_1}(k_0^{(n)}, k_{2r}^{(n)}))$  converges after 35 iterations. This difference can be explained by the many variables and dimensions that require more samples for accurate Kriging. However, at iteration 35, we notice that the Krigings are well precise, indeed  $\mathbb{E}(\widetilde{RMS}_{v_1}(k_0^{(n)}, k_{2r}^{(n)}))$  is within the confidence interval of  $\mathbb{E}(\widetilde{RMS}_{v_1}(k_0^{(n)}, k_{2r}^{(n)}))$ . Table 3 summarizes the results of the time-varying stiffness optimization.

Equilibrium points for the optimal varying stiffness are plotted in Fig. 13



(a)



(b)

Figure 12: Optimization results for the system with time-dependent nonlinearity: a) Optimal stiffness at each iteration  $k_0^{(n)}$  (black line with crosses) and  $k_{2r}^{(n)}$  (gray line with squares); b)  $\mathbb{E}(\widetilde{RMS}_{v_1}(k_0^{(n)}, k_{2r}^{(n)}))$  as a function of iterations for a time-varying nonlinearity and the parameters provided in Table 1. The results show a convergence after 35 iterations.

for several amplitudes of external excitation:  $f = 0.2$ ,  $f = 0.4$ ,  $f = 0.6$ , and  $f = 0.8$ .

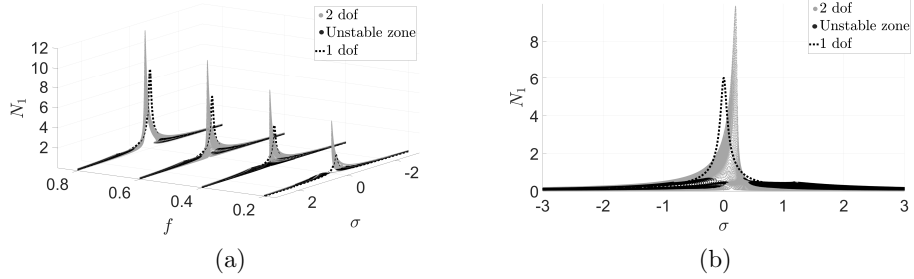


Figure 13: a) Equilibrium points for  $k_0 = 1.041$ ,  $k_{2r} = 0.435$  (optimal stiffness),  $f = 0.2, 0.4, 0.6, 0.8$ ; b) Equilibrium points for  $k_0 = 1.041$ ,  $k_{2r} = 0.435$   $f = 0.6$ . System parameters are reported in Table 1.

It should be mentioned that the equilibrium points of the system with time-dependent nonlinearity depicted in Fig. 13, are also phase-dependent ( $\delta_2$ ). That is why these figures present some areas due to the effect of the phase in another dimension [32]. As for the system with a constant nonlinearity, the equilibrium points illustrate the absorption capabilities of the system with the NES compared to the linear system. We can see that the equilibrium points of the 2 dof system are below those of the single dof system indicating the ability of the optimized NES to control the main system.

#### 4.4. Comparison between results of optimized designs of constant and time-dependent nonlinearities

The comparison of the results presented in Tables 2 and 3 reveals that  $\mathbb{E}(RMS_{v_1})$  at the optimum is lower for the system with time-dependent cubic nonlinearity than for the one with constant nonlinearity and is summarized in Table 4. This observation suggests that, under the chosen conditions, for the same mean excitation centered on the resonant frequency of the main system alone, the NES with a variable stiffness is more efficient, resulting in a reduction of 36% of the response of the main system.

The improved mitigation observed in the system with time-varying stiffness can be attributed to the parametric nature of the system. The variable stiffness introduces a frequency component that is twice the external frequency,

Stiffness	$\mathbb{E}(RMS_{v_1})$
Constant case	0.463
Variable case	0.298

Table 4: Comparison of optimization results with constant and variable nonlinearities.

with a phase shift of  $-\frac{\pi}{2}$ . This particular relationship leads to a significant response from the absorber, resulting in enhanced attenuation of the main system response [53, 65, 66]. Thus, the system acts as auto-parametric absorbers [67–69] including effects and interactions of higher harmonics than the main ones in the system (e.g. the second and fourth, Eq. 3).

## 5. Discussion

The presented optimization approach and methodology provide valuable information on mitigation of nonlinear systems using variable stiffness. However, the following aspects will require further investigation.

### 5.1. Clustering approach

Figure 6a illustrates multiple clusters corresponding to the main branch of the frequency response curve (equilibrium points), the unstable zone and the isola. Dividing the samples into two clusters is clear for an unforced system under different initial conditions. In this case, the clusters correspond to the activation of the NES [46]. However, for a forced system, the dynamics are more complex, and there exist discontinuities justifying the use of clusters. However, two clusters might not be sufficient. This work would require an optimal clustering strategy, which is beyond the scope of this article. A number of clusters corresponding to different response behaviors and amplitudes can lead to a more accurate approximation and take discontinuities better into account.

### 5.2. Sensitivity to initial conditions

In this article, the forced system under zero initial conditions is considered. Even though the 2 dof system reaches an isola with these conditions and thus exhibits the three different dynamics, non-zero initial conditions would allow it to reach an isola for more parameters. Additionally, considering the non-zero initial conditions could capture transient regimes during which the 2 dof system may have a rapid nonlinear decrease, while the single dof system presents linear mitigation.

### 5.3. Practical implementation

The 2 dof system could be used to model an acoustic mode of a tube coupled to a programmable electro-acoustic resonator [49, 50]. The actual dynamics of the membrane is more complex than the NES as presented in this article and could be modeled using, for instance, finite elements. However, the proposed optimization method for robust design would still be applicable.

## 6. Conclusion

The stochastic optimization of a NES with a time-varying nonlinear stiffness has been investigated. This system also corresponds to a practical application consisting of an acoustical mode of a tube coupled to a programmable electro-acoustic resonator.

The optimization problem is formulated so as to minimize the expected value of the ratio of RMS responses of the system with and without NES. The expected value is computed over a range of excitation amplitudes and frequencies. Because the system's response is highly sensitive to uncertainties and in fact exhibits discontinuities, a dedicated surrogate-based optimization approach was used. The optimization relies on the identification of clusters and the construction of several Kriging surrogates. Analytical developments were used to demonstrate the presence of discontinuities. The method is applicable to the robust optimization of any system including complex ones. The performance of the NES with time-varying nonlinear stiffness was compared to the case with constant stiffness. The initial results demonstrate that the proposed design leads to a better response attenuation than the constant stiffness case.

The optimization of time-varying stiffness designs will be further investigated to include additional sources of uncertainty, such as initial conditions, and design variables. Moreover, optimal clustering strategy should be considered for having more detailed insights about optimized designs.

## Acknowledgements

The authors would like to thank the following organizations for supporting this research: (i) The “Ministère de la transition écologique” and (ii) LABEX CELYA (ANR-10-LABX-0060) of the “Université de Lyon” within the program “Investissement d’Avenir” (ANR-11-IDEX-0007) operated by the French National Research Agency (ANR).

## Declaration

Conflict of interest: The authors declare that they have no conflict of interest.

## Appendix A. Details of parameters of the SIM

$$A = (-1 + \gamma_0) - \frac{N_2^2}{4} (4k_{2r} \cos(2\delta_2) + 4k_{2i} \sin(2\delta_2) - 3k_0 - k_{4r} \cos(4\delta_2) - k_{4i} \sin(4\delta_2)) \quad (\text{A.1})$$

$$B = \xi_2 - \frac{N_2^2}{4} (-2k_{2r} \sin(2\delta_2) + 2k_{2i} \cos(2\delta_2) + k_{4r} \sin(4\delta_2) - k_{4i} \cos(4\delta_2)) \quad (\text{A.2})$$

## Appendix B. Details of boundary of the unstable zone of the SIM

$$a_v = \frac{9}{64} (3k_0^2 - 2k_{2i}^2 - 2k_{2r}^2 - k_{4i}^2 - k_{4r}^2 + 4(-k_0 k_{2r} + k_{2i} k_{4i} + k_{2r} k_{4r}) \cos(2\delta_2) - 2(k_{2i}^2 - k_{2r}^2 + k_0 k_{4r}) \cos(4\delta_2) - 4(-k_{2r} k_{4i} + k_{2i}(k_0 + k_{4r})) \sin(2\delta_2) + 2(2k_{2i} k_{2r} - k_0 k_{4i}) \sin(4\delta_2)) \quad (\text{B.1})$$

$$b_v = \frac{3}{4} (-1 + \gamma_0) (k_0 - k_{2r} \cos(2\delta_2) - k_{2i} \sin(2\delta_2)) \quad (\text{B.2})$$

$$c_v = \frac{1}{4} ((-1 + \gamma_0)^2 + \xi_2^2) \quad (\text{B.3})$$

## References

- [1] M. Crocker. *Handbook of Noise and Vibration Control*. John Wiley & Sons, Ltd, 2007.
- [2] Z. Wani, M. Tantray, E. Noroozinejad Farsangi, N. Nikitas, M. Noori, B. S., T. Yang. A critical review on control strategies for structural vibration control. *Annual Reviews in Control*, 54:103-124, 2022.

- [3] D. Mead. *Passive vibration control*. Wiley, West Sussex, England, 1999.
- [4] S. Chu, T. Soong, A. Reinhorn. *Active, hybrid, and semi-active structural control: a design and implementation handbook*. Wiley, United Kingdom, 2005.
- [5] S. Korkmaz. A review of active structural control: challenges for engineering informatics. *Computers & Structures*, 89:2113-2132, 2011.
- [6] J. Den Hartog. *Mechanical Vibrations*. McGraw Hill, New York, 1934.
- [7] T. Furtmuller, G. Joas, C. Adam. Control of pendulum oscillations by tuned liquid dampers. *Journal of Fluids and Structures*, 114:103753, 2022.
- [8] H. Helmholtz. *On the sensations of tone as a physiological basis for the theory of music (in German: translated to English by A. J. Ellis)*. Braunschweig, Druck und Verlag von Friedrich Vieweg und Sons, Germany. Longmans, Greens, and Co., London, New York, Bombay and Calcutta., 1863 (in German), 1912 (in English: forth edition).
- [9] A. Komkin, M. Mironov, A. Bykov. Sound absorption by a helmholtz resonator. *Acoustical Physics*, 63:385-302, 2017.
- [10] R. Roberson. Synthesis of a nonlinear dynamic vibration absorber. *Journal of the Franklin Institute*, 254(3):205-220, 1952.
- [11] O. Gendelman, L. Manevitch, A. Vakakis, R. M'Closkey, Energy pumping in nonlinear mechanical oscillators: part i-dynamics of the underlying hamiltonian systems. *Journal of Applied Mechanics*, 68(1):34-41, 2001.
- [12] A. Vakakis, Inducing passive nonlinear energy sinks in vibrating systems. *Journal of Vibration and Acoustics*, 123(3):324-332, 2001.
- [13] S. Aubry, G. Kopidakis, A. Morgante, G. Tsironis. Analytic conditions for targeted energy transfer between nonlinear oscillators or discrete breathers. *Physica B: Condensed Matter*, 296(1-3): 222-236, 2001.
- [14] G. Kopidakis, S. Aubry, G. Tsironis. Targeted energy transfer through discrete breathers in nonlinear systems. *Physical review letters*, 87:165501, 2001.

- [15] J. Wu, I. Rudnick. Measurements of the nonlinear tuning curves of helmholtz resonators. *The Journal of the Acoustical Society of America*, 80(5):1419-1422, 1986 .
- [16] D. Innes, D. Crighton. On a non-linear differential equation modelling Helmholtz resonator response. *Journal of sound and vibration*, 131(2):323-330, 1989.
- [17] J. Keller, E. Zauner. On the use of helmholtz resonators as sound attenuators. *The Journal of Applied Mathematics and Physics (ZAMP)*, 46(3):297-327, 1995.
- [18] G. Yu, Y. Zhang, Y. Shen. Nonlinear amplitude-frequency response of a helmholtz resonator. *Journal of Vibration and Acoustics*, 133:024502, 2011.
- [19] V. Alamo Vargas, E. Gourdon, A. Ture Savadkoohi. Nonlinear softening and hardening behavior in helmholtz resonators for nonlinear regimes. *Nonlinear Dynamics*, 91(1):217-231, 2018.
- [20] E. Gourdon, A. Ture Savadkoohi, V. Alamo Vargas. Targeted energy transfer from one acoustical mode to an helmholtz resonator with nonlinear behavior. *Journal of Vibration and Acoustics*, 140(6):061005, 2018.
- [21] B. Cochelin, P. Herzog, P. Mattei. Experimental evidence of energy pumping in acoustics. *Comptes Rendus Mécanique*, 334(11):639-644, 2006.
- [22] R. Bellet, B. Cochelin, P. Herzog, P. Mattei. Experimental study of targeted energy transfer from an acoustic system to a nonlinear membrane absorber. *Journal of Sound and Vibration*, 329(14):2768-2791, 2010.
- [23] R. Bellet, B. Cochelin, R. Côte, P. Mattei. Enhancing the dynamic range of targeted energy transfer in acoustics using several nonlinear membrane absorbers. *Journal of Sound and Vibration*, 331:5657- 5668, 2012.
- [24] A. Vakakis, O. Gendelman, L. Bergman, D. McFarland, G. Kerschen, Y. Lee. *Nonlinear Targeted Energy Transfer in Mechanical and Structural Systems, I & II*. Solid Mechanics and Its Applications, Springer Netherlands, 2008.

- [25] B. Bergeot. Scaling law for the slow flow of an unstable mechanical system coupled to a nonlinear energy sink. *Journal of Sound and Vibration*, 503:116109, 2021.
- [26] F. Nucera, A. Vakakis, D. McFarland, L. Bergman, G. Kerschen. Targeted energy transfers in vibro-impact oscillators for seismic mitigation. *Nonlinear Dynamics*, 50(3):651-677, 2007.
- [27] O. Gendelman. Analytic treatment of a system with a vibro-impact nonlinear energy sink. *Journal of Sound and Vibration*, 331:4599-4608, 2012.
- [28] E. Gourc, G. Michon, S. Seguy, A. Berlioz. Targeted energy transfer under harmonic forcing with a vibro-impact nonlinear energy sink: Analytical and experimental developments. *Journal of Vibration and Acoustics*, 137(3), 2015.
- [29] M. Weiss, B. Vaurigaud, A. Ture Savadkoohi, C. Lamarque. Control of vertical oscillations of a cable by a piecewise linear absorber. *Journal of Sound and Vibration*, 435:281-300, 2018.
- [30] G. Hurel, A. Ture Savadkoohi, C.-H. Lamarque. Design of a nonlinear for a 2 degrees of freedom pendulum and experimental validation. *Structural Control and Health Monitoring*, 28(11):e2814, 2021.
- [31] C. da Silveira Zanin, A. Ture Savadkoohi, S. Baguet, R. Dufour, G. Hurel. Nonlinear vibratory energy exchanges in a meta-cell. *International Journal of Non-Linear Mechanics*, 146:104148, 2022.
- [32] A. Labetoulle, A. Ture Savadkoohi, E. Gourdon. Detection of different dynamics of two coupled oscillators including a time-dependent cubic nonlinearity. *Acta Mechanica*, 233:259-290, 2022.
- [33] C. Lamarque, A. Ture Savadkoohi, Z. Dimitrijevic. Dynamics of a linear system with time-dependent mass and a coupled light mass with nonsmooth potential. *Meccanica*, 49(1):135-145, 2014.
- [34] O. Gendelman. Targeted energy transfer in systems with non-polynomial nonlinearity. *Journal of Sound and Vibration*, 315(3):732-745, 2008.
- [35] L. Manevitch, O. Gendelman. *Tractable models of solid mechanics. Formulation, analysis and interpretation*. Springer-Verlag Berlin Heidelberg, 2011.

- [36] A. Ture Savadkoochi, C. Lamarque, M. Weiss, B. Vaurigaud, S. Charlemagne. Analysis of the 1:1 resonant energy exchanges between coupled oscillators with rheologies. *Nonlinear Dynamics*, 86, 2016.
- [37] J. Ginoux. Slow invariant manifolds of slow-fast dynamical systems. *International Journal of Bifurcation and Chaos*, 31(07)2150112, 2021.
- [38] T. Wang, Y. Tang, T. Yang, Z.-S. Ma, Q. Ding. Bistable enhanced passive absorber based on integration of nonlinear energy sink with acoustic black hole beam. *Journal of Sound and Vibration*, 544:117409, 2023.
- [39] S. Li, H. Wu, X. Zhou, T. Wang, W. Zhang. Theoretical and experimental studies of global dynamics for a class of bistable nonlinear impact oscillators with bilateral rigid constraints. *International Journal of Non-Linear Mechanics*, 133:103720, 2021.
- [40] S. Li, H. Wu, J. Chen. Global dynamics and performance of vibration reduction for a new vibro-impact bistable nonlinear energy sink. *International Journal of Non-Linear Mechanics*, 139:103891, 2022.
- [41] T. Wang, Y. Tang, X. Qian, Q. Ding, T. Yang. Enhanced nonlinear performance of nonlinear energy sink under large harmonic excitation using acoustic black hole effect. *Nonlinear Dynamics*, 111(14):12871-12898, 2023.
- [42] Y. Zhen, H. Li, Y. Tang. Novel vibration control method of acoustic black hole plates using active-passive piezoelectric networks. *Thin-Walled Structures*, 186:110705, 2023.
- [43] Y. Tang, G. Wang, T. Yang, Q. Ding. Nonlinear dynamics of three-directional functional graded pipes conveying fluid with the integration of piezoelectric attachment and nonlinear energy sink. *Nonlinear Dynamics*, 111(3): 2415-2442, 2023.
- [44] E. Boroson, S. Missoum. Optimization under uncertainty of parallel nonlinear energy sinks. *Journal of Sound and Vibration*, 394:451-464, 2017.
- [45] K. Marti. *Stochastic optimization methods. Stochastic Optimization Methods: Applications in Engineering and Operations Research*. Berlin, Heidelberg: Springer Berlin Heidelberg, 2015. 1-35.

- [46] E. Boroson, S. Missoum. Stochastic optimization of nonlinear energy sinks. *Structural and Multidisciplinary Optimization*, 55:633-646, 2017.
- [47] B. Aksoy, H. Shea. Multistable shape programming of variable-stiffness electromagnetic devices. *Science Advances*, 8(21):eabk0543, 2022.
- [48] E. De Bono, M. Morell, M. Collet, E. Gourdon, A. Ture Savadkoohi, M. Ouisse, C.H. Lamarque. Model-inversion control to enforce tunable Duffing-like acoustical response on an Electroacoustic resonator at low excitation levels. *Journal of Sound and Vibration*, 570:118070, 2024.
- [49] C. da Silveira Zanin, A. Labetoulle, E. De Bono, E. Gourdon, M. Collet, A. Ture Savadkoohi. Experimental evidences of nonlinear programmable electroacoustic loudspeaker. *Building Acoustics*, 30(3):249-263, 2023.
- [50] M. Morell, E. Gourdon, M. Collet, A. Ture Savadkoohi, E. De Bono, C.-H. Lamarque. Towards digitally programmed nonlinear electroacoustic resonators for low amplitude sound pressure levels: Modeling and experiments. *Journal of Sound and Vibration*, 584:118437, 2024.
- [51] L. Manevitch. The description of localized normal modes in a chain of nonlinear coupled oscillators using complex variables. *Nonlinear Dynamics*, 25:95-109, 2001.
- [52] V. Smirnov, L. Manevitch. Complex envelope variable approximation in nonlinear dynamics. *Russian Journal of Nonlinear Dynamics*, 16(3):491-515, 2020.
- [53] A. Nayfeh, D. Mook. *Nonlinear oscillations*. John Wiley & Sons, 2008.
- [54] Y. Starosvetsky, O. Gendelman. Strongly modulated response in forced 2dof oscillatory system with essential mass and potential asymmetry. *Physica D: Nonlinear Phenomena*, 237(13):1719-1733, 2008.
- [55] E. Boroson, S. Missoum. Reliability-based design optimization of nonlinear energy sinks. In *11th World congress of structural and multidisciplinary optimization. Sydney 2015* (pp. 750-757).
- [56] A. Vakakis, O. Gendelman, L. Bergman, D. McFarland, G. Kerschen, Y. Lee. Nonlinear targeted energy transfer in discrete linear oscillators with single-DOF nonlinear energy sinks. *Nonlinear Targeted Energy Transfer in Mechanical and Structural Systems*, 93-302, 2009.

- [57] C. Lamarque, A. Ture Savadkoochi, E. Etcheverria, Z. Dimitrijevic. Multi-scale dynamics of two coupled nonsmooth systems. *International Journal of Bifurcation and Chaos*, 22(12):1250295, 2012.
- [58] J. Kennedy. Particle Swarm Optimization. In: Sammut, C., Webb, G.I. (eds) *Encyclopedia of Machine Learning*. Springer, Boston (2011).
- [59] J. Hartigan, M. A. Wong. Algorithm AS 136: A k-means clustering algorithm. *Journal of the royal statistical society. series c (applied statistics)* 28(1):100-108, 1979.
- [60] J. Tou, R. Gonzalez. *Pattern recognition principles*. Addison-Wesley Publishing Company (1974).
- [61] V. Vapnik. *The nature of statistical learning theory*. Springer science & business media, 1999.
- [62] J. Shawe-Taylor, N. Cristianini. *Kernel methods for pattern analysis*. Cambridge university press, 2004.
- [63] S. Lacaze, S. Missoum. A generalized “max-min” sample for surrogate update. *Structural and Multidisciplinary Optimization* 49(4):683-687, 2014.
- [64] A. Basudhar, S. Missoum. An improved adaptive sampling scheme for the construction of explicit boundaries. *Structural and Multidisciplinary Optimization* 42:517-529, 2010.
- [65] D. Rugar, P. Grütter. Mechanical parametric amplification and thermo-mechanical noise squeezing. *Physical Review Letters* 67(6):699, 1991.
- [66] R. Lifshitz, M. Cross. Nonlinear dynamics of nanomechanical and micromechanical resonators. *Reviews of nonlinear dynamics and complexity* 1(1), 2008.
- [67] R. Haxton, A. Barr. The Autoparametric Vibration Absorber. *Journal of Engineering for Industry* 94(1):119-125, 1972.
- [68] A. VYAS, A. BAJAJ. Dynamics of autoparametric vibration absorbers using multiple pendulums. *Journal of Sound and Vibration* 246(1):115-135, 2001.

- [69] Z. Yan, H. Taha, T. Tan. Nonlinear characteristics of an autoparametric vibration system. *Journal of sound and vibration*, 390:1-22, 2017.